An in situ real-time growth study of Ag film on the ion beam sculptured GaSb nanostructures

Praveen Kumar Dubey [a,d], Sarath Sasi [b], Kumar Navin [c], Benedikt Sochor [d,e],
Stephan V. Roth [d,f], P.S. Anil Kumar [g], Ajay Gupta [a], Sarathlal Koyiloth Vayalil [a,d,*]

[a] *Department of Physics, UPES, Dehradun, Uttarakhand, India 248007*
[b] *New Technologies-Research Center, University of West Bohemia, Plzeň, Czech Republic*
[c] *Department of Physics, Maulana Azad National Institute of Technology, Bhopal, India*
[d] *Deutsches Elektronen-Synchrotron DESY, Notkestraße 85, 22607 Hamburg, Germany*
[e] *Advanced Light Source, Lawrence Berkeley National Laboratory, 6 Cyclotron Rd, Berkeley, CA 94720, USA*
[f] *Department of Fibre and Polymer Technology, KTH Royal Institute of Technology, Teknikringen 56, 10044 Stockholm, Sweden*
[g] *Department of Physics, Indian Institute of Science, Bangalore 560012, Karnataka, India*

ARTICLE INFO

ABSTRACT

Nanocone patterns with long-range order were fabricated on a GaSb (001) substrate using low-energy ion beam sputtering. The experimental findings elucidate the underlying mechanism involved in the growth of nanostructures on the GaSb (001) surface. These templates were used to study the growth dynamics of the Ag thin films through the in situ grazing incidence small angle X-ray scattering (GISAXS) technique. During film deposition, four distinct growth stages were observed: surface replication, cluster formation, coalescence into a continuous film, and shape transition of the nanoclusters from hemi-ellipsoids to cylinders after percolation. The GISAXS data and their simulations provided valuable insights into the film's structural evolution, shape, and distribution during deposition.

Introduction

Ion beam-assisted nanopatterning is emerging as a potential alternative to mask-free nanofabrication techniques for the preparation of self-organised nanostructures over a large surface area in a single step [1–9]. A wide variety of materials can be patterned into nanostructures with various shapes and sizes (ripples, dots, cones, mounds, etc.), which can be easily tuned by varying ion beam parameters, incorporating surfactant, and modifying the substrate conditions [3–8]. These nano-patterned surfaces are used as substrates for the deposition of thin films, nanowires, and nanodot arrays with wide applications spanning data storage, optoelectronics, nanoelectronics, biomedical devices, and plasmonics [10–14].

The process of self-organized patterns by ion beam irradiation is well explained by the Bradley-Harper (BH) model, with extensions based on recent theoretical and experimental research results [15–17]. The materials most commonly explored by various research groups for studying pattern evolution include metals, semiconductors, and amorphous materials. Among these, multi-component systems such as group III-V

semiconductors (e.g., GaSb) have gained significant theoretical and experimental interest due to the formation of dense, well-ordered arrays of nanodots, nanoripples, and nanocones [1,9,18–21]. Fascko et al. reported the formation of hexagonal dot arrays on a GaSb substrate under normal incidence of ion beam, while Allmers and co-workers observed a transition from dot to ripple patterns by varying the angle of incidence [1,22]. Various research groups have proposed distinct mechanisms for nanostructure growth in binary compounds, drawing on findings from their experimental and theoretical studies. Facsko et al. suggested that the preferential sputtering of one component (Sb) leads to surface instability, while a counter-surface diffusion mechanism results in the formation of nanodot structures on the GaSb substrate [9]. On the basis of compositional analysis, Le Roy et al. claimed that the segregation of the Ga atoms on the surface acts as a shield. This, combined with the preferential sputtering of Sb, leads to the formation of a dot-like nano-structure [23]. Bradley-Shipman proposed a theoretical model for binary compounds, stating that surface instability arises from a surface layer with an altered composition due to the preferential sputtering of one element (Sb), which triggers nanostructure formation in binary

---

* Corresponding author.
E-mail address: sarathlal.koyiloth.vayalil@desy.de (S. Koyiloth Vayalil).

compounds [17]. In contrast, Scott suggested that the phase separation of Ga (in the peak regions) and Sb (in valley regions), due to the preferential sputtering and redistribution of both elements, creates surface instability that drives the evolution of nanodot structures on the GaSb surface [24]. Interestingly, several in-situ studies on GaSb substrates have suggested a strong correlation between compositional variation and the growth of nanostructures in binary substrates [19–21]. Therefore, further exploration of the experimental processes is necessary to gain a clearer understanding of the actual growth mechanism.

Nanopatterned surfaces are primarily used as substrates for depositing metallic thin films with surface anisotropy, plasmonic nanowires, and nanodot arrays [25–31]. The ability to precisely control the morphology and distribution of the metal film on a nanopatterned surface is vital for achieving optimal device performance. In our previous work, we reported the detailed growth mechanisms and properties of magnetic thin films (cobalt and permalloy) on patterned substrates with ripple structures on the Si surfaces, exhibiting uniaxial magnetic anisotropy [26,28]. Giordano et al. highlighted the potential applications of PEDOT: PSS film on patterned glass substrates with enhanced anisotropic conductivity for organic nanoelectronics [10]. Barelli et al. demonstrated a remarkable enhancement in surface-enhanced Raman scattering (SERS) for gold films deposited on patterned glass substrates, enabling molecular and biosensing applications [13]. Oates and co-workers showed the application of ripple templates on Si surfaces to deposit silver nanoparticles for plasmonic application [29].

In this work, we report detailed investigations into the nanostructure evolution mechanism on the GaSb (001) surfaces under ion beam irradiation and the growth of Ag thin film on the patterned substrate using the in situ grazing incidence small angle X-ray scattering (GISAXS) technique. It is an advanced characterization method that allows real-time observation of the dynamic evolution of surface morphology and interface roughness during the deposition process [4]. By employing in-situ GISAXS, high-resolution temporal and spatial data on the nucleation and growth mechanisms of metallic thin films that interact with nanopatterned templates can be obtained. This insight guides the rational design and optimization of nanostructured materials, enabling the development of devices with tailored functionalities and improved performance.

Textured GaSb (001) templates with nanocone arrays were prepared using low-energy ion beams at normal incidence. The growth mechanisms of these nanostructures were examined using AFM and ex-situ GISAXS techniques. Further, the growth of Ag thin films on nanopatterned GaSb (001) templates has been investigated using in-situ GISAXS during deposition. Detailed information on the nucleation, growth, and coalescence processes of Ag thin films on the nanocone substrate were obtained from GISAXS measurements. The data revealed the evolution of Ag cluster size, shape, and distribution over deposition time. The scattering patterns exhibited distinct characteristics corresponding to the nanocone substrate and the Ag clusters, allowing precise determination of cluster size and interparticle spacing.
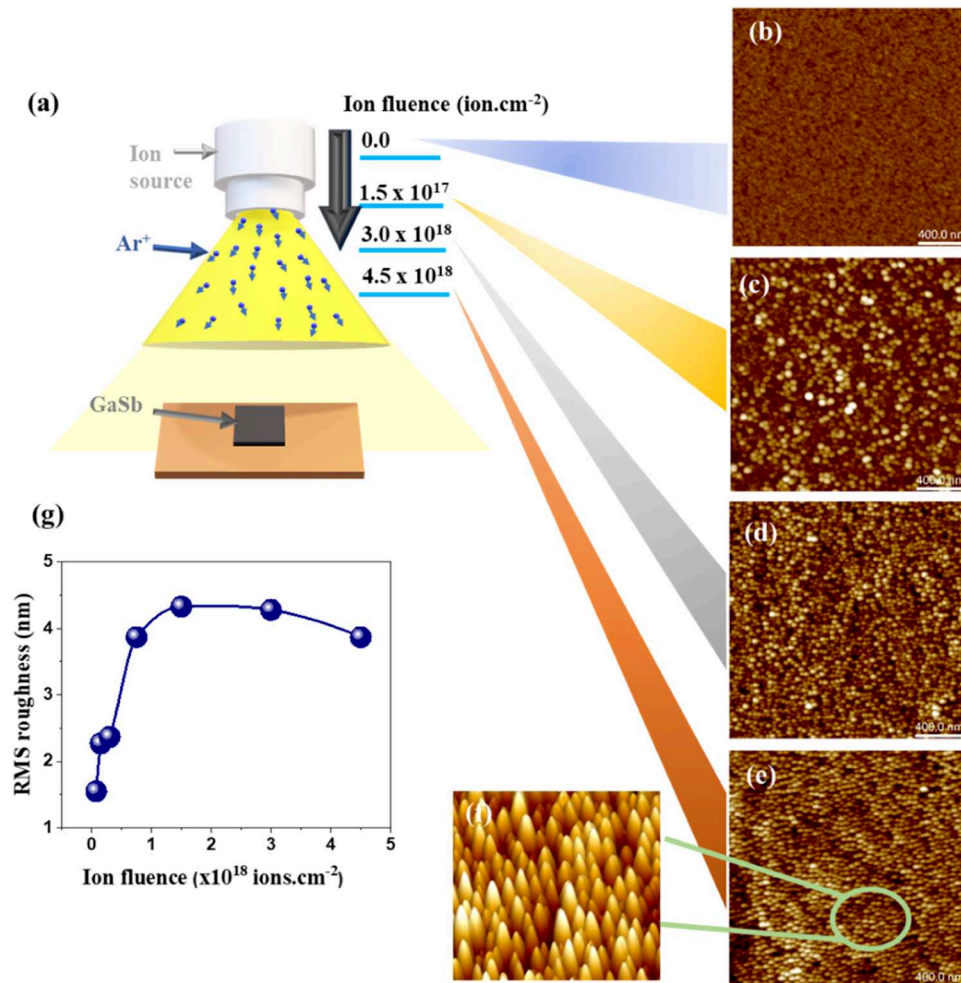

Fig. 1. (a) Schematic representation of the experimental setup used for the ion beam irradiation on the GaSb (001) substrate, (b-e) AFM images (2×2 μm) of GaSb (001) surfaces sputtered by the Ar^+ ion beam with different ion fluences (Φ), (f) enlarged image of Fig. 1 (e) and (g) variation of RMS roughness (*w*) with ion fluence.

2. Experimental details

Single-crystalline GaSb (001) substrates [5×5 mm^2, RMS roughness (σ) = 1.1 nm] were used for the preparation of the textured template by ion beam irradiation. The substrates were cleaned in an ultrasonic bath with acetone, isopropyl alcohol, and deionised (DI) water sequentially for 10 minutes. A schematic representation of the experimental setup is shown in Fig. 1 (a). The GaSb (001) substrate was irradiated at normal incidence using an Ar$^+$ ion beam with an energy of 400 eV. The experiment was carried out with a Kauffman-type hot cathode ion source (beam diameter: 3 cm) at a base pressure of 2×10^{-7} mbar, maintaining a constant ion flux value of 2.5×10^{15} ions.cm^{-2}.s^{-1}. The diameter of the ion beam was sufficiently large to cover the entire sample area. The surface morphology of the prepared templates was analysed using Atomic Force Microscopy (AFM, Nanoscope E, Digital Instruments) in tapping mode. AFM images were processed with Nanoscope analysis software available with the instrument and Gwyddion software [32] to extract detailed surface morphological parameters. RMS roughness (w), power spectral density (2D-PSD), and height-height correlation (HHCF) were extracted from AFM images to understand the growth behaviour and lateral distribution of nanostructures on the surface under different ion fluence [4,5,33].

Further detailed morphological characterization of the templates and Ag film growth on GaSb (001) (using highly automated sputter equipment) were performed using GISAXS with a microbeam at the MiNaXS/P03 beamline (PETRA III, DESY) [35–38]. GISAXS measurements with X-ray beam energy, beam size, and sample-to-detector distance for nanocone templates surface characterization- 12 KeV, 31×24 μm^2 (horizontal x vertical), 2851 ± 1 mm and during Ag film deposition- 11.83 KeV, 24×20 μm^2, 3240 ± 1 mm, were used respectively. PILATUS 1M (Dectris Ltd., Switzerland) with a pixel size of 172×172 μm^2 was used as a detector. Details of GISAXS scattering geometry during film deposition are explained in a later section. The deposition rate of the Ag thin film was maintained at 0.68 nm.min^{-1}, achieving a total thickness of 20.5 nm. The GISAXS data were analysed using the DPDAK program [34]. Selected 2D GISAXS plots were simulated under different growth regimes using the BornAgain program [39].

3. Results and discussion

(a) Evolution of nanocones on GaSb (001) substrate

Fig. 1 (b–e) shows the AFM images of the GaSb (001) samples irradiated with different ion fluence ranging from 1.5×10^{17} to 4.5×10^{18} ions.cm^{-2} at normal incidence. These images clearly illustrate the formation of nanocones on the GaSb (001) surface at lower fluences, which become more prominent at higher ion fluences. The enlarged AFM image of the irradiated surface with higher ion fluence [Fig. 1 (f)] clearly shows the formation of a nanocone-like structure with an average height of 16.7 nm. Fig. 1 (g) depicts the variation of RMS roughness with ion fluence.

The RMS roughness of the irradiated samples initially increases and then nearly saturates at higher ion fluences. For single-component substrates (such as Si or Ge), the surface remains smooth when irradiated at normal incidence, because of the dominant surface smoothening process. However, binary compounds have been observed to exhibit compositional instability near the surface region during ion beam irradiation, which contributes to nanostructure growth [19,40]. The surface roughness of pristine GaSb is attributed to the presence of native oxide on the surface. Keller et al. have also observed a transition from the smoothing to the roughening mechanism ($\Phi \leq 1.6 \times 10^{17}$ ions.cm^{-2}) in the GaSb (001) substrate under similar experimental conditions. Furthermore, they reported that the roughness nearly saturates at higher fluences [41].

Fig. 2 (a) shows the PSD curve of the GaSb (001) samples irradiated with different ion fluences. The PSD curve exhibits k-independent behaviour in the low-frequency region, while it decreases linearly in the high-frequency region. A peak near the cross-over region in the PSD curve indicates the periodicity of the nanostructure on the surface. The
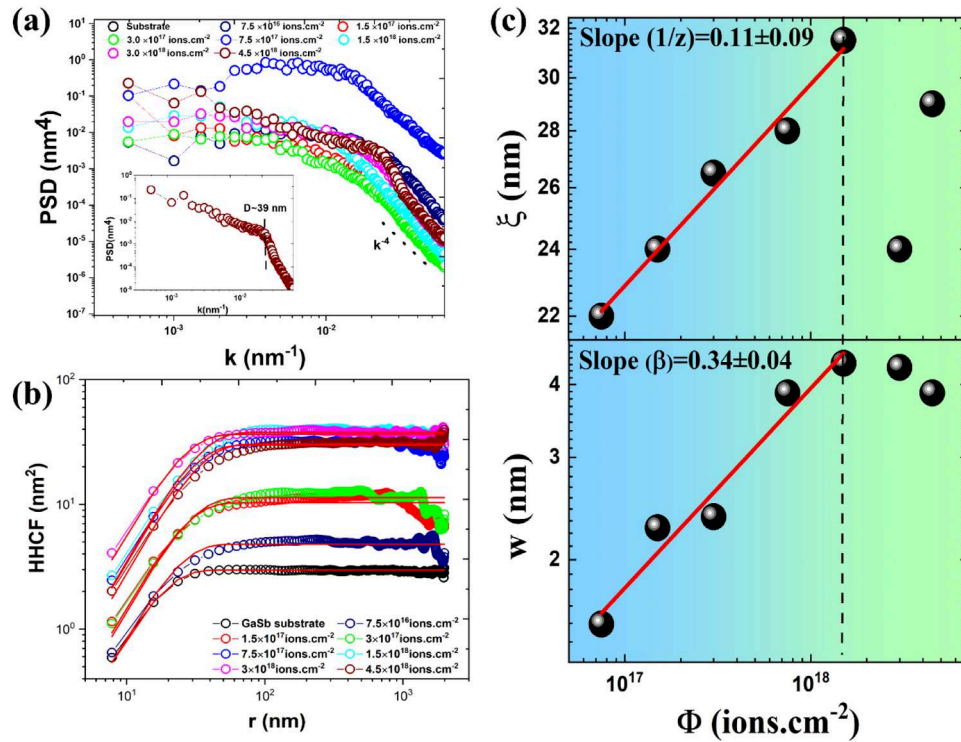

Fig. 2. (a) PSD curve of GaSb substrate irradiated with different ion fluence (Inset shows the PSD data of GaSb sample irradiated with ion fluence of 4.5×10^{18} ions.cm^{-2}), (b) HHCF calculated for GaSb samples irradiated with different ion fluence. (c) Variation of the length of the lateral correlation length (ξ) and the roughness of the RMS (w) with ion fluence (Φ) (log-log scale).

results do not show a peak in the PSD curve for all samples, except the surface irradiated with the highest ion fluence [inset of Fig. 2 (a)]. This indicates the presence of correlated structures on the surface with an average distance (D) of ~39 nm. Above cross-over frequency, it exhibits a power-law behaviour proportional to k^{-4}, suggesting ion-induced viscous flow as the dominant surface smoothing mechanism for all GaSb surfaces irradiated with different ion fluences [1,40]. The feature that appears in the high-frequency region is attributed to various noise sources.

Fig. 2 (b) shows the height-height correlation function [$H(r,t)$] calculated as a function of distance r on a log-log scale. The similar nature of the HHCF for different ion fluences indicates comparable roughening behaviour and uniform growth of nanostructures across fluences. The lateral correlation length (ξ) is obtained by fitting the HHCF curve, as shown in Fig. 2 (c). The increase in ξ with ion fluence indicates the lateral growth of nanostructures due to the formation of mounds or island-like structures, which becomes more pronounced with higher ion fluence [42]. These nanostructures likely evolve due to the agglomeration and aggregation of nanodots under ion beam irradiation. Dynamic exponent (z) is calculated by linear fitting of the ξ vs. Φ curve (log-log scale, $\xi \sim \Phi^{1/z}$) up to an ion fluence of 1.5×10^{18} ions.cm^{-2}.

The growth exponent (β) characterizes the surface roughening process and growth of the amplitude of the nanostructure with ion fluence. Fig. 2 (c) shows the variation in RMS roughness (w) with Φ, which closely follows the power law behaviour ($w \sim \Phi^{\beta}$) up to an ion fluence of 1.5×10^{18} ions.cm^{-2}. The value of β is calculated to be 0.34 ± 0.04, indicating the possibility of the role of nonlinear effects in the growth of nanostructure, which becomes more dominant at higher ion fluences. Further insight into the growth dynamics is obtained by calculating the roughness exponent γ ($\gamma = z.\beta$). The higher value of γ (i.e., $\gamma > 1$) indicates that the evolution of nanostructures in the vertical direction is more pronounced with ionic fluence compared to lateral growth [5,42].

A horizontal line cut through the two-dimensional GISAXS data [inset of Fig. 3 (a)] around the Yoneda region ($q_z = 0.62$ nm^{-1}) for all samples are shown in Fig. 3 (a) [4,43]. As fluence increases, the two-dimensional nature and the order of the samples interfere with the evolution of side peaks. The results indicate that the evolution of surface morphology occurs in two stages. The initial phase involves surface smoothing caused by irradiation, while the latter phase involves the formation of nanostructures, resulting in the appearance of lateral peaks. With increasing fluence, the full-width at half maximum (FWHM) of the lateral peaks decreases, indicating improved ordering. The correlation length of the pattern is also inversely proportional to the FWHM of the lateral peak [28].

On the basis of the analysis of the horizontal line cut, it can be observed that the order of the pattern increases as the ion fluence in-creases. Furthermore, as fluence increases, the lateral peaks shift towards a lower q-value, which is a manifestation of pattern coarsening. This shift corresponds to an increase in the distance between nanocones (D), which can be calculated using the given equation:

$$D = \frac{2\pi}{q_y} \qquad (i)$$

where q_y is the position of the side peak (scattering vector in y-direction). Fig. 3 (b) shows the variation of D with ion fluence, indicating that D increases from 22 nm to 37 nm with the increase in the fluence value from 7.5×10^{17} to 4.5×10^{18} ions.cm^{-2}, and tends towards saturation at higher fluences.

Recently, Lively et al. proposed a growth mechanism for nanostructures on a GaSb substrate through theoretical and experimental exploration based on nucleation and growth kinetics [18]. Since the sputtering yields of Ga and Sb are almost identical, they sputter at similar rates [19]. They observed that above a critical ion fluence, the nanostructure growth mechanism dominates over ion-induced surface smoothing. This process results in the formation of Sb "protoclusters" due to the high diffusional mobility of Sb near the surface region. These protoclusters attract other mobile Sb ions and form stabilised Sb clusters on the surface via nucleation and growth mechanisms.

The difference between the sputtering yield of GaSb surface phases and the laterally distributed Sb clusters drives the evolution of the nanostructure on the surface. Lively et al. also mentioned that the growth of nanostructure nearly saturates above a certain ion fluence or saturation fluence. Our experimental results align with this observation, showing that nanostructure formation begins above 7.5×10^{17} ions.cm^{-2} and growth nearly saturates above an ion fluence of 2.3×10^{18} ions.cm^{-2}.

(b) Growth of Ag thin film on patterned GaSb (001) substrate

A well-ordered GaSb nanocone substrate with $D = 23$ nm is used to deposit an Ag thin film. The schematic of the GISAXS scattering geometry during deposition is shown in Fig. 4 (a), where α_i, α_f, and $2\theta_f$ denote the incident, exit, and scattering angles, respectively. 2D GISAXS images for selected Ag film thickness values, $t = 0, 1, 2, 4, 6$ and 20 nm, are shown in Fig. 4 (b), where q_y and q_z represent the scattering vectors along y and z directions. Y_{Ag} and Y_{GaSb} represent the Yoneda peak positions of Ag and GaSb, respectively. The position of the Yoneda peak always corresponds to $\alpha_f = \alpha_c$, where α_f is the exit angle and α_c is the critical angle. The peak position can be calculated using the formula [43, 45]:

$$Y = \frac{2\pi}{\lambda}(\sin \alpha_c + \sin \alpha_i) \qquad (ii)$$
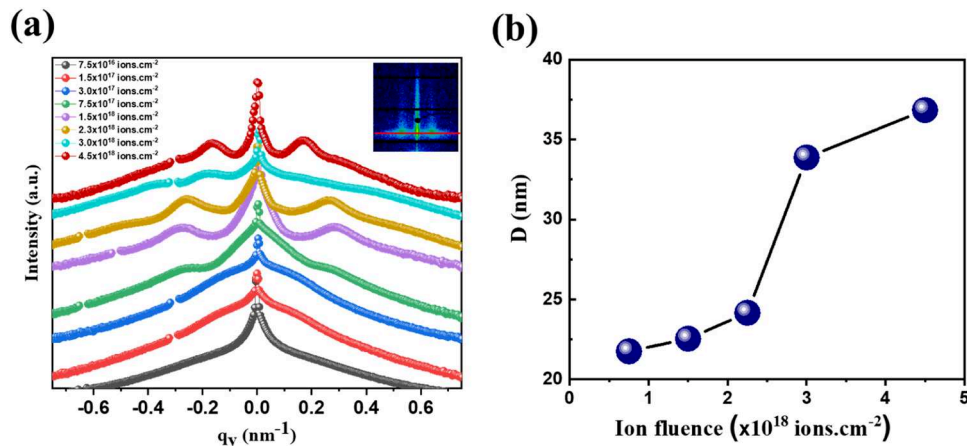

Fig. 3. (a) GISAXS horizontal line cut along the q_y direction at fixed q_z position (Yoneda) peak of the GaSb, (b) Variation of average inter-particle distance between particles (D) with ion fluence.
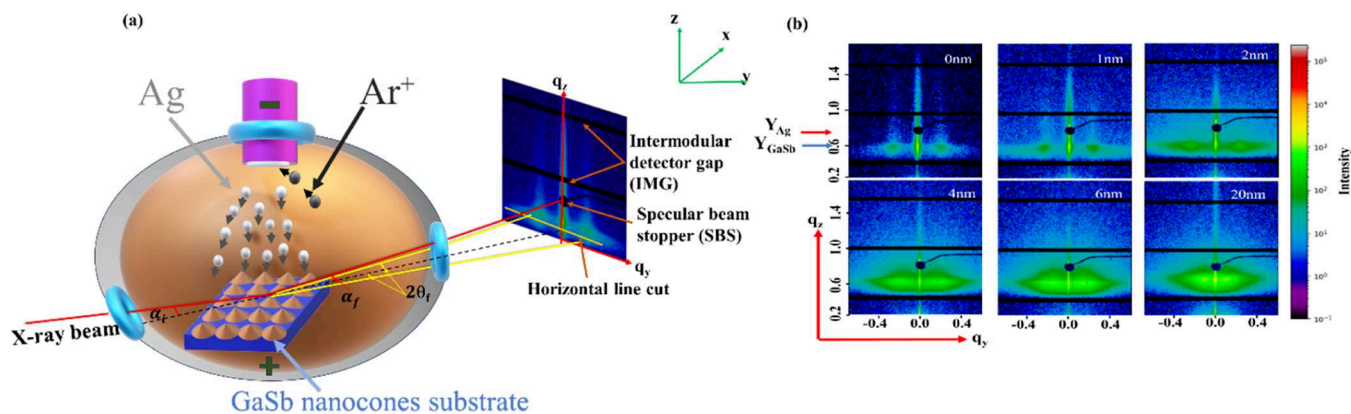
Fig. 4. (a) Schematic of GISAXS scattering geometry during sputter deposition. (b) 2D GISAXS images for selected Ag thickness values. Yoneda peak of Ag (Y_{Ag}) and Yoneda peak of GaSb (Y_{GaSb}) are shown by red and blue arrows, respectively.

where λ is the wavelength of the X-ray beam. Furthermore, α_c can be determined using the equation $\alpha_c = \sqrt{2\delta}$, where δ is the refractive index decrement related to the effective electron density.

Fig. 5 (a). shows horizontal line integrations plotted at fixed $q_z = 0.67$ nm^{-1} (between Y_{GaSb} and Y_{Ag}) for Ag film thickness values ranging from 0 to 20.5 nm, to get information about the evolution of lateral correlations in the system. A side peak at $q_y = 0.26$ nm^{-1}, corresponding to the correlated structure of GaSb nanocones, remains at the same position during the early film thickness regime. As the thickness of the film increases, the side peak corresponding to Ag clusters shifted from higher q values to lower q values, indicating an increase in real space separation between the Ag clusters [38,45]. To analyse the variation in the position and FWHM of the side peaks with film thickness, peak fitting is performed using a symmetric double Lorentzian (LODS) function, which is commonly used to analyse the peak shapes of X-ray scattering and diffraction data [34,44].

This function combines two Lorentzian functions and can be mathematically expressed as:

$$L(x) = \frac{|A|}{1 + \left(\frac{x - pos}{\frac{FWHM}{2}}\right)^2} + \frac{|A|}{1 + \left(\frac{x + pos}{\frac{FWHM}{2}}\right)^2} \qquad \text{(iii)}$$

where x is an independent variable over which the Lorentzian function is evaluated, A is the amplitude of the Lorentzian peaks, pos is the position parameter that determines the centre of each Lorentzian peak, and $FWHM$ is the full width at half maxima of the Lorentzian peaks. Fig. 5 (b) shows the variation in the side peak positions of GaSb and Ag with increasing film thickness. For very thin films (a few angstroms thick), the peak position of Ag appears around $q_y = 2$ nm^{-1}, indicating the initial formation of Ag nanoclusters with an average intercluster distance of approximately 3 nm, calculated using equation(i). As the film thickness increases, the Ag peak position rapidly decreases towards lower q_y values and becomes constant after 6 nm. At around 1.5 nm thickness, the Ag side peak merges with the GaSb side peak, indicating that the interparticle separation of Ag clusters matches the inter-particle separation of GaSb nanocones.

Fig. 5 (c) shows the variation in the FWHM of side peaks corresponding to GaSb and Ag with increasing Ag film thickness. The FWHM of the Ag side peak decreases exponentially, whereas the FWHM of the GaSb side peak remains almost constant up to a thickness of 1.5 nm and then increases with further film thickness. The reduction in FWHM of the Ag peak with increasing thickness suggests that the lateral distribution of the material becomes more uniform as the thickness of the film increases [28]. The FWHM variations of the Ag side peak can be further analysed using two functions: an exponential decay function and a linear
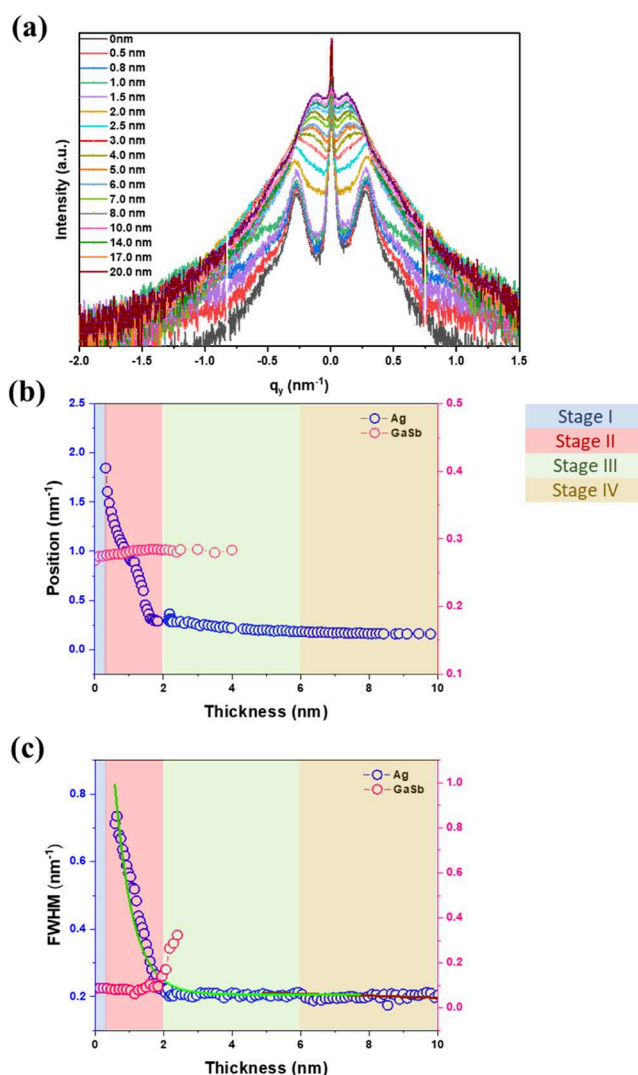

Fig. 5. (a) Horizontal line cuts are extracted at $q_z = 0.67$ nm^{-1} for a film thickness ranging from 0 to 20 nm. (b) A 2D graph shows the relationship between the lateral correlations' peak position with Ag thickness (represented by blue circles) and GaSb (represented by pink circles). (c) FWHM of the side peaks of GaSb and Ag are plotted with increasing Ag film thickness. Four growth regimes are indicated with different colours.

function (shown by the green and wine colour lines, respectively). The intersection of the two functions occurs at a film thickness of approximately 6 nm, which closely corresponds to the percolation threshold reported in earlier studies [38,44,45].

Fig. 6 presents a 2D image for thicknesses of 0.4, 1.0, 5.0 and 12.0 nm, along with their corresponding simulation images and models. Simulation of GISAXS patterns was conducted to represent the time evolution of the cluster shape and lateral distribution, highlighting the physical significance of our approach [46]. The cluster distribution was described using distorted-wave Born approximation [46,47]. The analysis was carried out by implementing an analytical computation method that used a 2D paracrystal interference function. In addition, a hexagonal arrangement was used to describe the lateral packing of the clusters. The following four growth stages were observed:

(a) Stage I: The replication stage, where Ag atoms replicate the unique topographical features of the GaSb nanocone substrate by coating its contours up to a few angstroms thick.

(b) Stage II: One of the primary influences on Ag growth is the difference in surface free energy between GaSb (0.5–0.7 J·m^{-2}) and Ag (1.2–1.4 J·m^{-2}). Since Ag has a higher surface free energy, its atoms tend to minimize their exposure to the substrate by bonding preferentially with one another. This strong Ag-Ag interaction is further reinforced by Ag's high cohesive energy (2.95 eV/atom), which stabilizes the formation of discrete clusters instead of promoting uniform adhesion to the GaSb surface. Consequently, the weak adhesion between Ag and GaSb inhibits smooth film formation, favouring the growth of isolated Ag islands [48–50].

Another key factor contributing to the clustering behaviour is the large lattice mismatch (~33 %) between Ag (4.09 Å) and GaSb (6.10 Å). This significant mismatch introduces considerable strain energy at the Ag/GaSb interface, making layer-by-layer growth energetically unfavourable. Instead of forming a continuous thin film, Ag follows the Volmer-Weber (VW) growth mode, where atoms nucleate into three-dimensional islands to minimize strain energy [51,52].

Furthermore, the deposition process leads to Sb segregation at the surface, altering the local chemical environment. The presence of segregated Sb reduces the wettability of Ag, further discouraging uniform layer formation and reinforcing island growth. The combination of weak adhesion, high cohesive energy, lattice mismatch, and surface segregation ultimately dictates that Ag does not spread uniformly on GaSb but instead forms discrete clusters, particularly between adjacent nanocones where surface energy effects are enhanced [50,51].
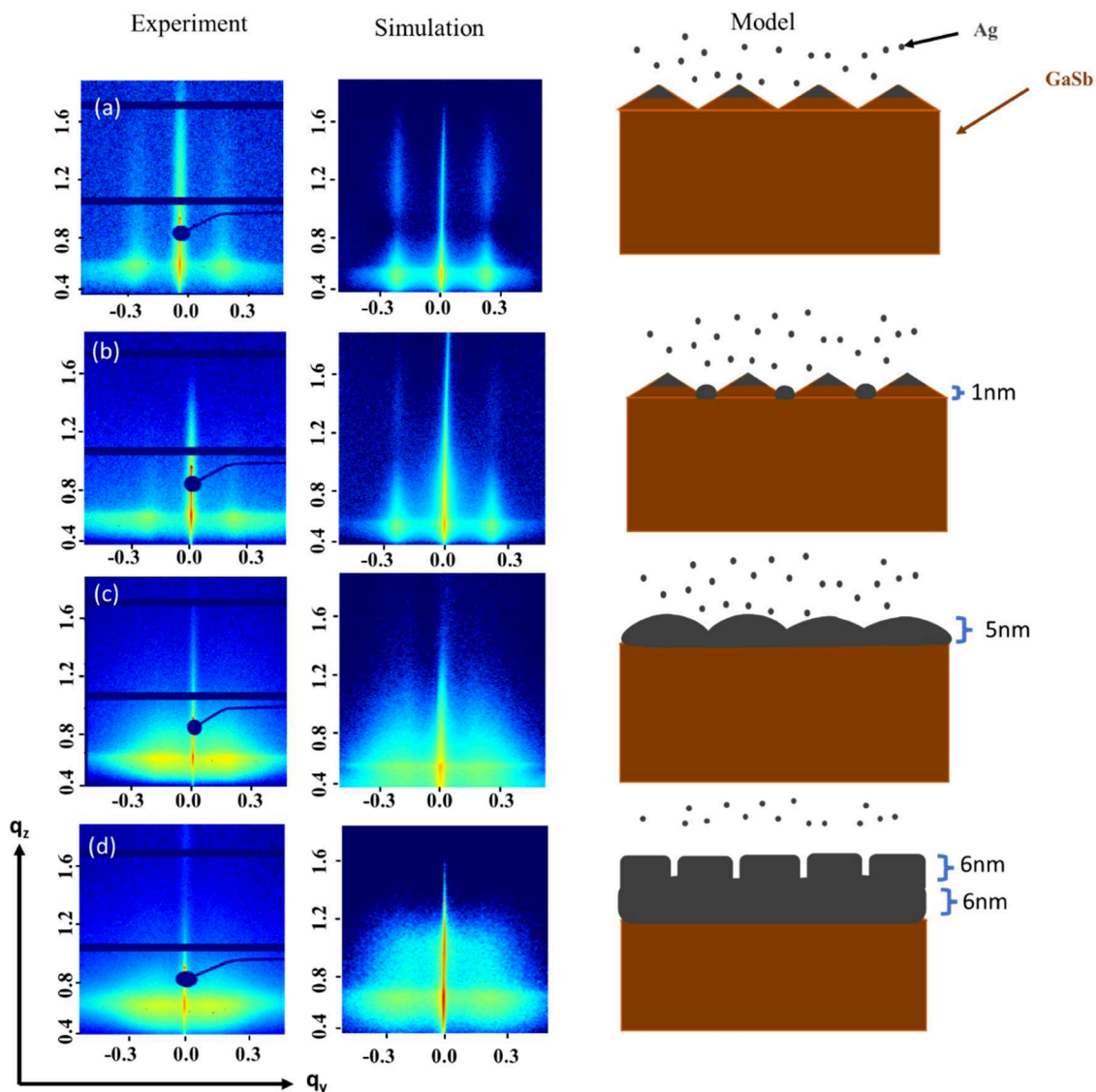

Fig. 6. Experimental and simulation images of the 2D GISAXS data with their model for the different film thicknesses of (a) 0.4 nm, (b) 1.0 nm, (c) 5.0 nm, and (d) 12.0 nm.

(c) Stage III: This stage marks the transition to a more ordered arrangement of clusters, as reflected in the FWHM progression shown in Fig. 5 (c).

Stage IV: The shape of the Ag clusters changes from hemi-ellipsoidal to more elongated cylindrical structures. This occurs as Ag is predominantly adsorbed onto the Ag base layer once percolation is achieved, consistent with observations from previous work [44].

For the simulations, a cone-shaped structure was used in stage I, with particles arranged in a core-shell configuration: the core representing the GaSb nanocones and the shell comprising Ag atoms. In stages II and III, a hemi-ellipsoidal shape was used for the Ag clusters, alongside a core-shell model. In stage IV, the Ag nanoclusters exhibited a different growth pattern, as indicated by the progression of FWHM in Fig. 5 (c). At this stage, the Ag atoms were more likely to collide with preexisting nanoclusters rather than the bare surface. To ensure agreement between the data and simulations, a cylindrical model was adopted after percolation.

4. Conclusion

We examined the evolution of the GaSb surface morphology, which was observed to occur in two main stages: the first stage involves irradiation-induced surface smoothening, while the second stage involves the formation of nanocones. Nanostructure formation was observed to start above an ion fluence of 7.5×10^{17} ions.cm^{-2} and its growth nearly saturates above 2.3×10^{18} ions.cm^{-2}. The average distance between two nanocones increases as the ion fluence increases. Furthermore, we investigated the in situ real-time evolution of Ag cluster growth on a GaSb nanocone template (average intercone separation of 23 nm) using the GISAXS technique. The obtained data show that Ag cluster growth occurs in four broad stages: initial surface replication, followed by small cluster formation, continuous grain growth, and a shape transition from hemi-ellipsoidal to cylindrical structures upon passing the percolation threshold. We presented a geometric model based on simulation to validate our hypothesis for the different growth stages of Ag thin film deposition on a GaSb nanocone substrate. The primary characteristics, including position, shape, and relative intensity at various maxima, were successfully replicated. These results are relevant for potential applications in plasmonics, nanofabrication, and other advanced material systems where surface morphology plays a critical role in determining functional properties.

CRediT authorship contribution statement

Praveen Kumar Dubey: Writing – original draft, Methodology, Investigation, Formal analysis, Data curation. **Sarath Sasi:** Writing – original draft, Methodology, Formal analysis. **Kumar Navin:** Writing – original draft, Methodology, Formal analysis, Data curation. **Benedikt Sochor:** Visualization, Resources, Methodology, Formal analysis. **Stephan V. Roth:** Methodology, Investigation, Conceptualization. **P.S. Anil Kumar:** Supervision, Resources, Formal analysis. **Ajay Gupta:** Writing – review & editing, Supervision, Investigation, Formal analysis. **Sarathlal Koyiloth Vayalil:** Writing – review & editing, Writing – original draft, Visualization, Validation, Supervision, Software, Resources, Methodology, Investigation, Funding acquisition, Formal analysis, Data curation.

Declaration of competing interest

The authors declare that they have no known competing financial interests or personal relationships that could have appeared to influence the work reported in this paper.

Acknowledgement

Data availability

Data will be made available at a reasonable request.

References

[1] S. Facsko, T. Dekorsy, C. Koerdt, C. Trappe, H. Kurz, A. Vogt, H.L. Hartnagel, Formation of ordered nanoscale semiconductor dots by ion sputtering, Sci 285 (1999) 1551–1553, https://doi.org/10.1126/science.285.5433.1551.

[2] A. Deka, P. Barman, M.K. Mukhopadhyay, S.R. Bhattacharyya, Influence of metal codeposition on the growth and orientation of nanoripple structure during ion bombardment, Phys. Rev. B 105 (2022) 195437, https://doi.org/10.1103/PhysRevB.105.195437.

[3] Rakhi, J. Muñoz-García, R. Cuerno, S. Sarkar, Towards ordered Si surface nanostructuring: role of an intermittent ion beam irradiation approach, Phys. Scr. 98 (2023) 055902, https://doi.org/10.1088/1402-4896/acc618.

[4] S.K. Vayalil, A. Gupta, S.V. Roth, V. Ganesan, Investigation of the mechanism of impurity assisted nanoripple formation on Si induced by low energy ion beam erosion, J. Appl. Phys. 117 (2015) 024309, https://doi.org/10.1063/1.4905684.

[5] K. Navin, A. Gupta, S.K. Vayalil, Molybdenum assisted self-organized pattern formation by low energy ion beam sputtering, Appl. Phys. A. 130 (2024) 316, https://doi.org/10.1007/s00339-024-07466-y.

[6] A. Keller, S. Facsko, Tuning the quality of nanoscale ripple patterns by sequential ion-beam sputtering, Phys. Rev. B 82 (2010) 155444, https://doi.org/10.1103/PhysRevB.82.155444.

[7] K. Steeves Lloyd, I.L. Bolotin, M. Schmeling, L. Hanley, I.V. Veryovkin, Metal impurity-assisted formation of nanocone arrays on Si by low energy ion-beam irradiation, Surf. Sci. 652 (2016) 334–343, https://doi.org/10.1016/j.susc.2016.03.016.

[8] D. Erb, R. de Schultz, A. Ilinov, K. Nordlund, R.M. Bradley, S. Facsko, Nanopatterning of the (001) surface of crystalline Ge by ion irradiation at off-normal incidence: experiment and simulation, Phys. Rev. B 102 (2020) 165422, https://doi.org/10.1103/PhysRevB.102.165422.

[9] S. Facsko, H. Kurz, T. Dekorsy, Energy dependence of quantum dot formation by ion sputtering, Phys. Rev. B 63 (2001) 165329, https://doi.org/10.1103/PhysRevB.63.165329.

[10] M.C. Giordano, F. di Sacco, M. Barelli, G. Portale, F. Buatier de Mongeot, Self-organized tailoring of faceted glass nanowrinkles for organic nanoelectronics, ACS Appl. Nano Mater. 4 (2021) 1940–1950, https://doi.org/10.1016/j.apsusc.2018.02.163.

[11] D. Repetto, M.C. Giordano, A. Foti, P.G. Gucciardi, C. Mennucci, F. Buatier de Mongeot, SERS amplification by ultra-dense plasmonic arrays on self-organized PDMS templates, Appl. Surf. Sci. 446 (2018) 83–91, https://doi.org/10.1016/j.apsusc.2018.02.163.

[12] D.P. Datta, T. Som, Strongly antireflective nano-textured Ge surface by ion-beam induced self-organization, Sol. Energy 223 (2021) 367–375, https://doi.org/10.1016/j.solener.2021.05.016.

[13] M. Barelli, M.C. Giordano, P.G. Gucciardi, F. Buatier de Mongeot, Self-organized nanogratings for large-area surface plasmon polariton excitation and surface-enhanced raman spectroscopy sensing, ACS Appl. Nano Mater. 3 (2020) https://doi.org/10.1021/acsanm.0c01569, 8784–8793.

[14] C. Mennucci, S. Del Sorbo, S. Pirotta, M. Galli, L.C. Andreani, C. Martella, M. C. Giordano, F. Buatier de Mongeot, Light scattering properties of self-organized nanostructured substrates for thin-film solar cells, Nanotech 29 (2018) 355301, https://doi.org/10.1088/1361-6528/aac9ac.

[15] R.M. Bradley, J.M.E. Harper, Theory of ripple topography induced by ion bombardment, J. Vacu. Sci. & Tech. A: Vacu., Surf. Film. 6 (1988) 2390–2395, https://doi.org/10.1116/1.575561.

[16] F.C. Motta, P.D. Shipman, R.M. Bradley, Highly ordered nanoscale surface ripples produced by ion bombardment of binary compounds, J. Phys. D: Appl. Phys. 45 (2012) 122001, https://doi.org/10.1088/0022-3727/45/12/122001.

[17] P.D. Shipman, R.M. Bradley, Theory of nanoscale pattern formation induced by normal-incidence ion bombardment of binary compounds, Phys. Rev. B 84 (2011) 085420, https://doi.org/10.1103/PhysRevB.84.085420.

[18] M.A. Lively, B. Holybee, M. Toriyama, S. Facsko, J.P. Allain, Nonlinear compositional and morphological evolution of ion irradiated GaSb prior to nanostructure formation, Sci. Rep. 10 (2020) 8253, https://doi.org/10.1038/s41598-020-64971-9.

[19] O. El-Atwani, J.P. Allain, A. Cimaroli, A. Suslova, S. Ortoleva, The significance of *in situ* conditions in the characterization of GaSb nanopatterned surfaces via ion beam sputtering, J. Appl. Phys. 110 (2011) 074301, https://doi.org/10.1063/1.3642997.

[20] O. El-Atwani, J.P. Allain, S. Ortoleva, In-situ probing of near and below sputter-threshold ion-induced nanopatterning on GaSb(100), Nucl. Instru. and Methods in Phys. Res. Sec. B: Beam Interac. with Mater. and Atoms 272 (2012) 210–213, https://doi.org/10.1016/j.nimb.2011.01.067.

[21] O. El-Atwani, S. Gonderman, J. Paul Allain, Near sputter-threshold GaSb nanopatterning, J. Appl. Phys. 114 (2013) 104308, https://doi.org/10.1063/1.4820261.

[22] T. Allmers, M. Donath, G. Rangelov, Pattern formation by erosion sputtering on GaSb: transition from dot to ripple formation and influence of impurities, J. Vacu. Sci. & Tech. B: Microelectro. Nanometer Struc. Process., Measur., Phenom. 24 (2006) 582–586, https://doi.org/10.1116/1.2170100.

[23] S.Le Roy, E. Søndergård, I.S. Nerbø, M. Kildemo, M. Plapp, Diffuse-interface model for nanopatterning induced by self-sustained ion-etch masking, Phys. Rev. B 81 (2010) 161401, https://doi.org/10.1103/PhysRevB.81.161401.

[24] S.A. Norris, Ion-assisted phase separation in compound films: an alternate route to ordered nanostructures, J. Appl. Phys. 114 (2013) 204303, https://doi.org/10.1063/1.4833551.

[25] S. KV, D. Kumar, V. Ganesan, A. Gupta, In-situ study of magnetic thin films on nanorippled Si (100) substrates, Appl. Surf. Sci. 258 (2012) 4116–4121, https://doi.org/10.1016/j.apsusc.2011.07.105.

[26] S. KV, D. Kumar, A. Gupta, Growth study of Co thin film on nanorippled Si(100) substrate, Appl. Phys. Lett. 98 (2011) 123111, https://doi.org/10.1063/1.3567731.

[27] S. Koyiloth Vayalil, A. Gupta, S.V. Roth, V. Ganesan, Investigation of the mechanism of impurity assisted nanoripple formation on Si induced by low energy ion beam erosion, J. Appl. Phys. 117 (2015) 024309, https://doi.org/10.1063/1.4905684.

[28] S. Koyiloth Vayalil, A. Koorikkat, A.K. Gopi, S.V. Roth, P.S. Anil Kumar, Tailoring of uniaxial magnetic anisotropy in Permalloy thin films using nanorippled Si substrates, J. Phys.: Condens. Matter 32 (2020) 185804, https://doi.org/10.1088/1361-648X/ab6d0d.

[29] T.W.H. Oates, A. Keller, S. Noda, S. Facsko, Self-organized metallic nanoparticle and nanowire arrays from ion-sputtered silicon templates, Appl. Phys. Lett. 93 (2008) 063106, https://doi.org/10.1063/1.2959080.

[30] M. Ranjan, S. Facsko, M. Fritzsche, S. Mukherjee, Plasmon resonance tuning in Ag nanoparticles arrays grown on ripple patterned templates, Microelect. Engineer. 102 (2013) 44–47, https://doi.org/10.1016/j.mee.2012.02.018.

[31] A.K. Bera, A.S. Dev, M. Kuila, M. Ranjan, P. Pandit, M. Schwartzkopf, S.V. Roth, V.R. Reddy, D. Kumar, Morphology induced large magnetic anisotropy in obliquely grown nanostructured thin film on nanopatterned substrate, Appl. Surf. Sci. 581 (2022) 152377, https://doi.org/10.1016/j.apsusc.2021.152377.

[32] D. Nečas, P. Klapetek, Gwyddion: an open-source software for SPM data analysis, Open Phys. 10 (2012) 181–188, https://doi.org/10.2478/s11534-011-0096-2.

[33] A. Deka, P. Barman, M.K. Mukhopadhyay, S.R. Bhattacharyya, Transition of nano-ripple to nano-hillock pattern on ion bombarded Si with an enhanced hydrophobicity, Surf. Interf. 25 (2021) 101242, https://doi.org/10.1016/j.surfin.2021.101242.

[34] G. Benecke, W. Wagermaier, C. Li, M. Schwartzkopf, G. Flucke, R. Hoerth, I. Zizak, M. Burghammer, E. Metwalli, P. Müller-Buschbaum, M. Trebbin, S. Förster, O. Paris, S.V. Roth, P. Fratzl, A customizable software for fast reduction and analysis of large X-ray scattering data sets: applications of the new *DPDAK* package to small-angle X-ray scattering and grazing-incidence small-angle X-ray scattering,

[35] A. Buffet, A. Rothkirch, R. Döhrmann, V. Körstgens, M.M. Abul Kashem, J. Perlich, G. Herzog, M. Schwartzkopf, R. Gehrke, P. Müller-Buschbaum, S.V. Roth, P03, the microfocus and nanofocus X-ray scattering (MiNaXS) beamline of the PETRA III storage ring: the microfocus endstation, J. Synchrotron. Rad. 19 (2012) 647–653, https://doi.org/10.1107/S0909049512016895.

[36] M. Schwartzkopf, S. Roth, Investigating polymer–metal interfaces by grazing incidence small-angle X-ray scattering from gradients to real-time studies, Nanomaterials 6 (2016) 239, https://doi.org/10.3390/nano6120239.

[37] R. Döhrmann, S. Botta, A. Buffet, G. Santoro, K. Schlage, M. Schwartzkopf, S. Bommel, J.F.H. Risch, R. Mannweiler, S. Brunner, E. Metwalli, P. Müller-Buschbaum, S.V. Roth, A new highly automated sputter equipment for *in situ* investigation of deposition processes with synchrotron radiation, Rev. Sci. Instru. 84 (2013) 043901, https://doi.org/10.1063/1.4798544.

[38] M. Schwartzkopf, A. Buffet, V. Körstgens, E. Metwalli, K. Schlage, G. Benecke, J. Perlich, M. Rawolle, A. Rothkirch, B. Heidmann, G. Herzog, P. Müller-Buschbaum, R. Röhlsberger, R. Gehrke, N. Stribeck, S.V. Roth, From atoms to layers: in situ gold cluster growth kinetics during sputter deposition, Nanoscale 5 (2013) 5053, https://doi.org/10.1039/c3nr34216f.

[39] G. Pospelov, W. Van Herck, J. Burle, J.M. Carmona Loaiza, C. Durniak, J.M. Fisher, M. Ganeva, D. Yurov, J. Wuttke, *BornAgain* : software for simulating and fitting grazing-incidence small-angle scattering, J. Appl. Crystallogr. 53 (2020) 262–276, https://doi.org/10.1107/S1600576719016789.

[40] J. Zhou, S. Facsko, M. Lu, W. Moeller, Nanopatterning of Si Surfaces by Normal Incident Ion Erosion: Influence of Metal Incorporation on Surface Morphology Evolution, 2010, https://doi.org/10.48550/ARXIV.1002.1002.

[41] A. Keller, A. Biermanns, G. Carbone, J. Grenzer, S. Facsko, O. Plantevin, R. Gago, T. H. Metzger, Transition from smoothing to roughening of ion-eroded GaSb surfaces, Appl. Phys. Lett. 94 (2009) 193103, https://doi.org/10.1063/1.3136765.

[42] A. Deka, P. Barman, G. Bhattacharjee, S.R. Bhattacharyya, Evolution of ion-induced nano-dot patterns on silicon surface in presence of seeding materials, Appl. Surf. Sci. 526 (2020) 146645, https://doi.org/10.1016/j.apsusc.2020.146645.

[43] Y. Yoneda, Anomalous surface reflection of X rays, Phys. Rev. 131 (1963) 2010–2013, https://doi.org/10.1103/PhysRev.131.2010.

[44] M. Schwartzkopf, A. Hinz, O. Polonskyi, T. Strunskus, F.C. Löhrer, V. Körstgens, P. Müller-Buschbaum, F. Faupel, S.V. Roth, Role of sputter deposition rate in tailoring nanogranular gold structures on polymer surfaces, ACS Appl. Mater. Interface. 9 (2017) 5629–5637, https://doi.org/10.1021/acsami.6b15172.

[45] S. Yu, G. Santoro, Y. Yao, D. Babonneau, M. Schwartzkopf, P. Zhang, S.K. Vayalil, P. Wessels, R. Döhrmann, M. Drescher, P. Müller-Buschbaum, S.V. Roth, Following the island growth in real time: Ag nanocluster layer on Alq3 thin film, J. Phys. Chem. C 119 (2015) 4406–4413, https://doi.org/10.1021/jp512675w.

[46] A. Nejati, M. Svechnikov, J. Wuttke, BornAgain, software for GISAS and reflectometry: releases 1.17 to 20, EPJ Web Conf. 286 (2023) 06004, https://doi.org/10.1051/epjconf/202328606004.

[47] D.H. Madison, R.V. Calhoun, W.N. Shelton, Triple-differential cross sections for electron-impact ionization of helium, Phys. Rev. A 16 (1977) 552–562, https://doi.org/10.1103/PhysRevA.16.552.

[48] W. Liu, W.T. Zheng, Q. Jiang, First-principles study of the surface energy and work function of III-V semiconductor compounds, Phys. Rev. B 75 (2007) 235322, https://doi.org/10.1103/PhysRevB.75.235322.

[49] L. Vitos, A.V. Ruban, H.L. Skriver, J. Kollár, The surface energy of metals, Surf. Sci. 411 (1998) 186–202, https://doi.org/10.1016/S0039-6028(98)00363-X.

[50] S. Walters, R. Williams, The interaction of Ag with the clean and oxidized n-type GaSb(110) surfaces, Vacuum 38 (1988) 325–328, https://doi.org/10.1016/0042-207X(88)90070-X.

[51] R.H. Williams, Semiconductor surfaces and interfaces, Vacuum 33 (1983) 587–592, https://doi.org/10.1016/0042-207X(83)90577-8.

[52] I. Lindau, T. Kendelewicz, N. Newman, R.S. List, M.D. Williams, W.E. Spicer, Electronic properties of metal/III–V semiconductor interfaces, Surf. Sci. 162 (1985) 591–604, https://doi.org/10.1016/0039-6028(85)90953-7.